Materials & Design 227 (2023) 111765

Contents lists available at ScienceDirect

Materials & Design

journal homepage: www.elsevier.com/locate/matdes

Characterization of mechanical properties of five hot-pressed lignins extracted from different feedstocks by microscopy-aided nanoindentation

Michael Schwaighofer [a,*], Luis Zelaya-Lainez [a], Markus Königsberger [a], Markus Lukacevic [a], Sebastián Serna-Loaiza [b], Michael Harasek [b], Olaf Lahayne [a], Valentin Senk [a], Josef Füssl [a]

[a] Institute for Mechanics of Materials and Structures, TU Wien, Karlsplatz 13/202, Vienna 1040, Vienna, Austria
[b] Institute of Chemical, Environmental and Bioscience Engineering, TU Wien, Getreidemarkt 9/166, Vienna 1040, Vienna, Austria

HIGHLIGHTS

- Lignin is tested using light-microscopy-aided grid nanoindentation.
- Micromechanics-based evaluation yields a reliable elastic modulus of 7.1 GPa.
- The mechanical properties neither depend on the feedstock nor the extraction process.

GRAPHICAL ABSTRACT

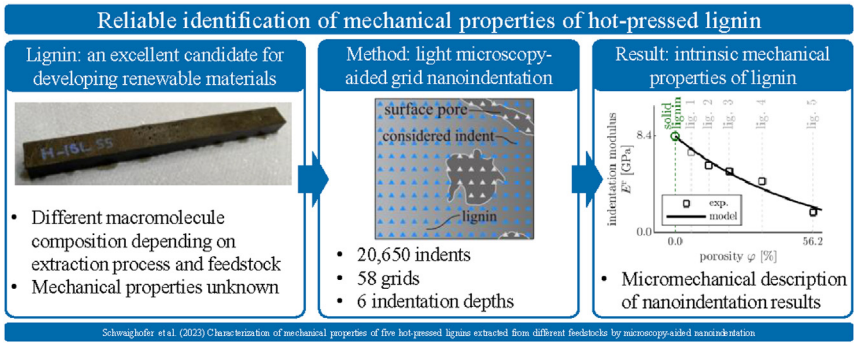

ARTICLE INFO

Article history:
Received 3 October 2022
Revised 19 January 2023
Accepted 16 February 2023
Available online 25 February 2023

Keywords:
Young's modulus
Hardness
Stiffness
Experiments
Micromechanics
Porous

ABSTRACT

Lignin, a main component of plants, is produced in large quantities as a by-product of the pulp and paper-making industry. The abundance of this organic polymer makes it an excellent candidate for developing renewable materials such as lignin-based biocomposites. The mechanical properties of lignin, as well as the dependence on the extraction process and feedstock, are, however, still unknown and hamper its utilization. Therefore, five hot-pressed lignins, extracted by different processes from different feedstocks, are tested by means of grid nanoindentation at indentation depths ranging from 150 nm to 1200 nm. Statistical and microstructure-guided evaluation based on microscopy images of the indented areas allows for retrieving reliable indentation properties of the porous lignin, free of indentation size effects. The sought mechanical properties of the solid (pore-free) lignin are back-identified from the strong correlation between the property and the porosity using micromechanics homogenization theory. This correlation reveals that the solid lignin in all tested samples is mechanically similar, despite different chemical structures, with a virtually intrinsic Young's modulus of 7.1 GPa.

1. Introduction

Lignin, a main component of plants, is the second most common organic natural material on the planet [1]. Despite this abundance, and despite the availability of lignin as an unwanted by-product of

* Corresponding author.
E-mail address: michael.schwaighofer@tuwien.ac.at (M. Schwaighofer).

https://doi.org/10.1016/j.matdes.2023.111765
0264-1275/

the pulp and paper-making industry [2,3], only a minor fraction of this renewable and sustainable material is used mainly for low-value applications, e.g., as a lubrification agent in the coal industry, as fertilizer or soil conditioner in agriculture, as a water-reducing agent in concrete, or as grinding aid in the cement industry [4,5]. Most of the lignin, however, is currently still burned as low-quality fuel [6]. Only recently, biorefineries have targeted lignin valorization [7], and an increasing effort is made to find new ways to utilize lignin as a renewable resource, e.g., as a cationic emulsifier in bitumen emulsions [8], to produce carbon foams [9], as a component in composites [3,10–13], and as an absorbent for lead ion removal [14].

The lignin extracted from lignocellulosic biomass, so-called "technical" lignin, is a rather diverse product. Lignin is a three-dimensional amorphous polymer consisting of three basic phenylpropane units, i.e., p-coumaryl alcohol, coniferyl alcohol, and syringyl alcohol [2]. The ratios of the phenylpropane units in the lignin vary depending on the plant species. Softwood lignin mainly consists of coniferyl alcohol, hardwood lignin is composed of coniferyl and syringyl alcohol, whereas grass lignin is made of p-coumaryl, coniferyl, and syringyl alcohol [1,2,5]. The properties and structure of native lignin, as it occurs in plants, change during the extraction and separation process [15]. In the kraft process, the biomass is treated with sodium sulfide and hydroxide [16], changing the functional groups [17]. Technical lignin, similar to native lignin, can be extracted with the organosolv process, which uses organic solvents [16]. Other standard extraction processes are sulfite and soda pulping [1,16].

In contrast to the manufacturing processes and the chemical composition, little attention has been paid to the mechanical properties of lignin (in all its variants), despite their importance, e.g., for the development of lignin-based biocomposite materials. The Young's modulus, a measure of the material stiffness, was quantified experimentally on hot-pressed technical lignin by means of continuous ball indentation tests [18,19] or tensile and torsion tests [20], on embedded lignin particles using atomic force microscopy [21–23], or on wood samples, particularly in lignin-rich cell corners of the middle lamella, using nanoindentation [24–26], see the compilation in Table 1. Moreover, molecular dynamics simulations [27–30] were performed to quantify the elastic moduli of lignin in bamboo and softwood. The tests and models reveal a wide range of Young's moduli from 1.5 to 14.8 GPa. Some of this variety has been linked to different moisture contents [19–22,28,29], different oxidation states [22], and different extraction methods [19]. The question of whether the chemical differences from the different feedstocks and different extraction processes translate to different mechanical properties can, however, not be answered satisfactorily, given the different quantification methods on differently prepared specimens of very different size and the fact that almost all papers (except [19,20] studies from the 70s) focus on a single lignin type, i.e., one specific feedstock/extraction method).

This provides the motivation for the present paper, where we aim at enabling a proper comparison of different technical lignins, extracted by different methods from different feedstocks. Grid nanoindentation [31,32] is used, given that it allows us to perform many tests in reasonable time at the required small scales. Additionally, nanoindentation enables us to measure the indentation hardness, a quantity which, so far, has not been reported in the literature on technical lignin. By testing at several different indentation depths, we aim at retrieving reliable mechanical quantities, which do not suffer from indentation size effects [33–36]. The nanoindentation tests are enriched by image analyses of microscopic images, allowing us to examine the indented areas, and correlate the measurements to microstructural features, most notably, to the specimen production-related porosity. Micromechanics is then used to quantify the mechanical properties of all tested solid (i.e., pore-free) lignins.

2. Materials and methods

2.1. Materials and sample preparation

Four commercially available lignins (labeled E-HW, OS-G, OS-HW, and K-SW, respectively) and one "in–house" produced lignin (labeled OS-SW) were tested. Two lignins were extracted from softwood (OS-SW and K-SW), two from hardwood (OS-HW and E-HW), and one from grass (OS-G) using Kraft pulping (K-SW), organosolv (OS-G, OS-HW, and OS-SW), and enzyme hydrolysis (E-HW), see Table 2 for a compilation and Appendix A for more details on the extraction process of the non-commercial OS-SW lignin. The purity of the lignins was assessed by the Klason lignin content, which was determined as acid-soluble lignin (ASL) and acid-insoluble lignin (AIL) according to the NREL/TP-510–42618 [37]. AIL was evaluated by a gravimetric method and ASL by UV/VIS absorption at 205 nm using a Shimadzu UV-1800 spectrophotometer. It is noteworthy that the Klason lignin content of K-SW[1] amounts to only 17.6 % and thus is significantly lower than the roughly 90 % found for the other lignins.

The five lignin powders were hot-pressed to obtain specimens that can be tested by means of nanoindentation. In more detail, the lignin powders were put in a pre-heated custom-made hydraulic pressing system and subjected to 108 MPa of pressure for 2 min at 90 °C to produce discs with a radius of approximately 10 mm and a height of about 10 mm. After that, the lignin discs were embedded into a 2-component resin (Struers, Denmark) and attached to a microscope slide.

The samples' surfaces were smoothed by means of a rotating diamond head attached to an ultra milling-sectioning system (Leica, Germany). The surface roughness of the samples was determined by means of a Hysitron Triboindenter TI900 in scanning probe mode (SPM) within homogeneous sample regions without pores. Before each topology and indentation testing, the indenter tip geometry was calibrated using fused quartz as a reference. The RMS roughness R_q is smaller than $R_q \leqslant 40$ nm for all samples, see Table 3 for details.

2.2. Nanoindentation testing

Displacement-controlled nanoindentation tests were performed in grids by means of a Hysitron TI900 Triboindenter with an attached diamond Berkovich tip at a constant relative humidity of 35 %. The load history consists of loading at a constant rate in 10 sec to the maximum indentation depth h_{max}, a short plateau with constant displacements held for 5 sec, and unloading at a constant rate in, yet again, 10 sec, see Fig. 1. Nanoindentation test results, particularly of polymers to which lignin may be comparable, are expected to exhibit a significant size-effect, i.e., indentation properties are expected to depend on the indentation depth [33,34,38–40]. As a remedy, grid nanoindentation was performed at six different depths, with h_{max} ranging from 150 nm to 1200 nm, see Table 3 for details. This way, the chosen indentation depths are at least 5 times larger than the measured surface roughness R_q. The indentation protocol thus obeys the requirement of a smooth and flat surface [41]. The upper limit of h_{max} is defined by the maximum force of 12000 μN of the triboindenter.

[1] As for the comparison of the properties of the K-SW lignin with the other lignins, this chemical difference has to be kept in mind, which is why the K-SW lignin is displayed in gray rather than blue, used for the other four lignins, throughout the following figures.

Table 1
Young's moduli of lignin found in the literature.

Reference	Determination method[☆]	Feedstock	Extraction method	Specimen	Young's Modulus [GPa]	Note
[18]	BI	Pinus radiata	Dioxane	hot-pressed cylinder (d = 4.8 mm)	3.3	
[20]	TaT	Pinus radiata	Klason and periodate	hot-pressed cylinder ($h/d = 20/4.6$ mm)	1.2 to 6.7	Influence of moisture content and extraction method
[19]	BI	Pinus radiata	Dioxane, Klason and periodate	hot-pressed cylinder ($h/d = 7/4.6$ mm)	1.7 to 6.6	Influence of moisture content and extraction method
[21]	AFM		Kraft (K-SW)	particle < 250 μm	2.4 to 9.0	Influence of moisture content
[22]	AFM	Maize stalks (Zea mays L.)	Dioxane	film (57 nm)	5.8 to 14.8	Range due to oxidation and different relative humidity
[23]	AFM	Softwood	Kraft (E-HW Finland)	particle	1.5	
[27,28]	MD	Bamboo			4.2 to 6.2	Influence of moisture content
[29]	MD	Softwood			2.5 to 3.7	Variation of moisture content
[30]	MD	Softwood			1.9	
[24]	Ni in ML	Picea abies		cuboid (2/2.5/1.5 mm)	7.1 ± 1.18	Hardness 0.43 ± 0.09 GPa
[25]	Ni in ML	Picea rubens Sarg.		cuboid (1 mm^2)	6.9 ± 2.26	
[26]	Ni in ML	Norway OS-SW (Picea abies)		cuboid ($10^4/10^4$/ 200 μm)	7.5	Hardness 0.42 GPa

[☆]Determination methods: continuous ball indentation tests (BI), tensile and torsion tests (TaT), atomic force microscopy (AFM), molecular dynamics simulations (MD), nanoindentation of cell corner middle lamella (Ni in ML).

Table 2
Lignin producer, product, extraction process, feedstock, and Klason lignin content.

	E-HW	OS-G	OS-HW	OS-SW	K-SW
Producer	Not reported	Chemical Point	Fraunhofer Center for Chemical-Biotechnological Processes	This work	Sigma Aldrich
Product name	Not reported	Chemical Point Lignin	Organosolv Lignin	Not Applicable	Alkali Lignin
Extraction process	Enz. Hydrolysis	Organosolv	Organosolv	Organosolv	Kraft pulping
Feedstock category	Hardwood	Grass	Hardwood	Softwood	Softwood
Feedstock	Beech	Corn silk, ballon flower	Beech	OS-SW	Mixture of spruce and pine
Klason lignin [wt. %]	86.4	93.7	88.4	90.0	17.6

Indents were performed in one or several grids such that at least 100 but up to 2450 individual locations were tested, see Table 3. The distance between the indents was selected such that neighboring indents did not influence each other [31], i.e. the ratio

Table 3
Nanoindentation testing campaign: surface roughness R_q, maximum indentation depth h_{max}, and grid size.

E-HW $R_q = 25$ nm						
h_{max} [nm]	150	300	600	900	1000	1200
Number of indents	1600	850	100	100	100	100
Grid	40 × 40	34 × 25	4 × 5 × 5	4 × 5 × 5	4 × 5 × 5	4 × 5 × 5
OS-G $R_q = 40$ nm						
h_{max} [nm]		300	600	900	1000	1200
Number of indents		850	200	200	200	200
Grid		34 × 25	2 × 10 × 10	2 × 10 × 10	2 × 10 × 10	2 × 10 × 10
OS-HW $R_q = 21$ nm						
h_{max} [nm]	150	300	600	900	1000	1200
Number of indents	1600	850	100	100	100	100
Grid	40 × 40	34 × 25	4 × 5 × 5	4 × 5 × 5	4 × 5 × 5	4 × 5 × 5
OS-SW $R_q = 25$ nm						
h_{max} [nm]	150	300	600	900	1000	1200
Number of indents	1600	2450	1600	1600	1600	1600
Grid	40 × 40	40 × 40 34 × 25	40 × 40	40 × 40	40 × 40	40 × 40
K-SW $R_q = 30$ nm						
h_{max} [nm]	150	300	600	900	1000	1200
Number of indents	1600	850	100	100	100	100
Grid	40 × 40	34 × 25	10 × 10	10 × 10	10 × 10	10 × 10

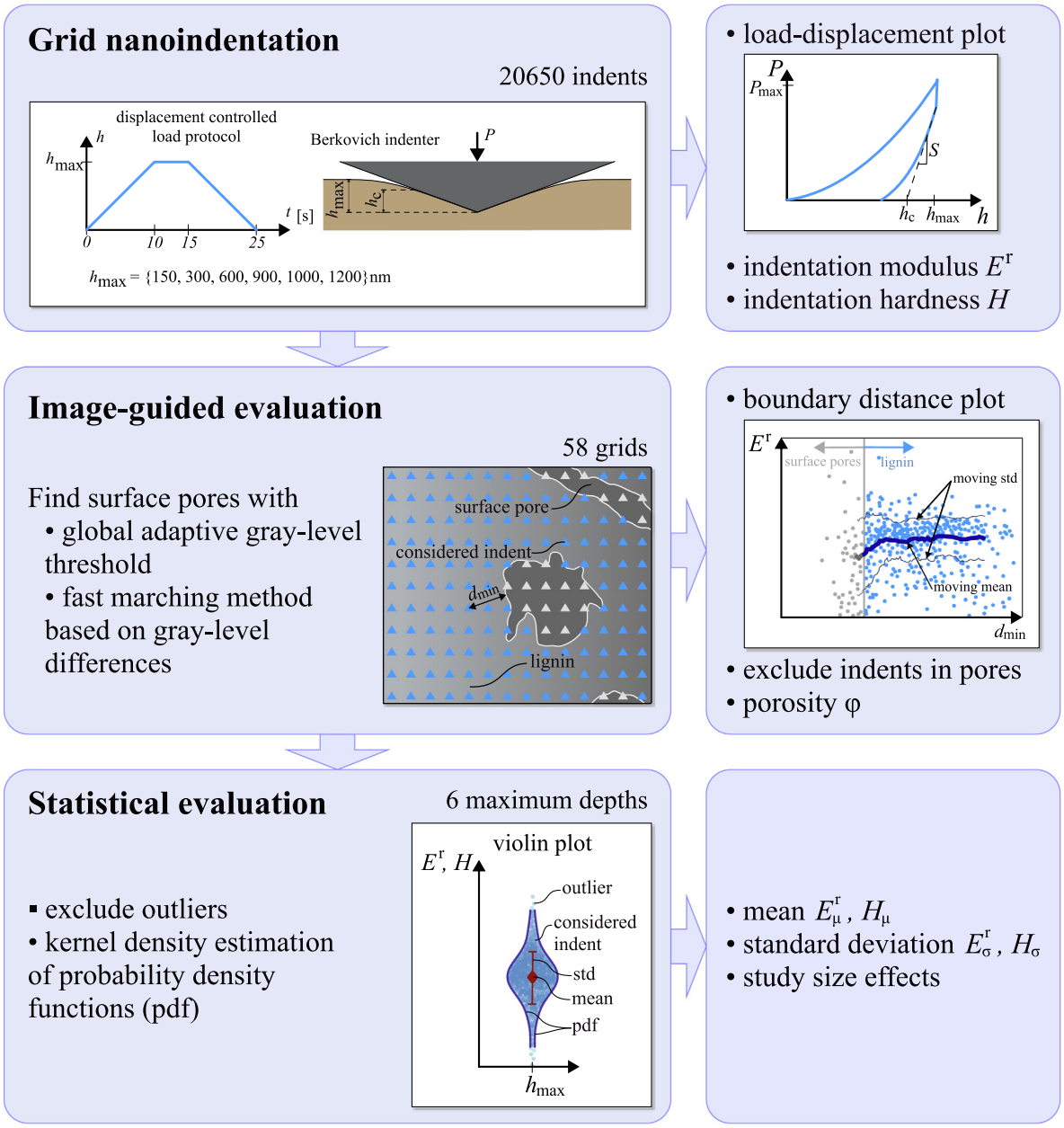

Fig. 1. Nanoindentation testing and evaluation strategy.

between indentation depth h_{max} and grid distance amounted to 12.5 or larger.

The measured force–displacement curves (*P*-*h* diagrams) are evaluated by means of the Oliver–Pharr method [32], as commonly done in indentation testing [31]. This yields indentation moduli E^r and hardnesses H. Notably, the quantified indentation modulus E^r is the result of elastic deformations of both, the lignin specimen *and* the diamond indenter tip, hence

$$\frac{1}{E^r} = \frac{1-\nu_i^2}{E_i} + \frac{1-\nu_s^2}{E_s}, \tag{1}$$

with Young's modulus E_s and Poisson's ratio ν_s of the specimen, and with Young's modulus $E_i = 1141$ GPa and Poisson's ratio $\nu_i = 0.07$ of the diamond indenter tip [32]. Additional information on the application of the Oliver–Pharr method is provided in the Supplementary material Appendix B.

2.3. Image-guided evaluation

The mechanical data obtained from indentation testing are accompanied by light microscopy images, taken by the in-built camera system, with a resolution of 640 times 480 pixels for an area of about 990 times 727 μm^2. Despite careful specimen preparation, the hot-pressed lignin samples exhibited a rather substantial porosity, see the dark gray areas in Fig. 1. To adequately evaluate the indentation results, this porosity needs to be quantified, as described next.

The pores on the surface are identified semi-automatically. First, a global adaptive gray level threshold is used [42]. Given the inhomogeneous lighting of the images, with brigthly illuminated areas in the center but darker areas on the rim, this method produces inadequate porosity distributions. To improve the results, a point in an unrecognized, but obvious, surface pore is manually picked as a seed. A fast marching method [43], using Matlab [44],

is then adopted based on gray level differences to isolate the pore, in which the seed is located. This way, the lignin-specific porosity φ is obtained as the area fraction of the (automatically detected and the manually picked) surface pores. Thereby, the images at a depth of 300 nm and 600 nm for OS-G and 150 nm and 300 nm for the remaining lignins are considered, because they display the largest area.

Indents located inside the surface pores should not be considered, given that this area is not polished and thus not flat. The therein-measured indentation properties suffer from structural effects (imperfect half space, non-orthogonality of load direction, and specimen surface). To identify the corresponding indents, the indent positions are mapped onto the microscopic image exploiting the identity between the grid center and image center. Notably, indents of the outermost rows and columns of the grid, directly at the border, are not considered either, given that only a part of the surrounding is visible.

The modulus and hardness obtained from indents inside the solid part are, very likely, still affected by pores (visible pores on the indented surface but also pores below the surface), particularly for indents which are in "close" proximity to the solid-pore border. Microstructural heterogeneities are "felt" even if they are surprisingly far away from the indent [45], particularly if the contrast in stiffness/hardness is substantial [46], and thus particularly for porous composites dealt with herein. To analyze the influence, we follow [45] and quantify the distance $d_{\min}$ between each indent and the *closest* border of any surface pore (see Fig. 1 for an illustration) and study possible correlations with the measured indentation quantities. Only pores with an area larger than 100 pixels = 234 μm^2 are thereby considered, given that the smaller ones barely influence the indentation results. Additional images of the pore modulus correlation are shown in the Supplementary material Appendix B.

2.4. Statistical evaluation

The indentation quantities (modulus and hardness) from all indents in the grid which are located outside of the pores and not on the outer edge are then evaluated statistically. First, outliers, defined as data points which are 1.5 times the interquartile range ($E^{\mathrm{r}}_{\mathrm{IQR}}$ for the indentation modulus and $H^{\mathrm{r}}_{\mathrm{IQR}}$ for the indentation hardness) above the upper and below the lower (modulus or hardness) quartile, respectively, are removed from the indents, individually for all six indentation depths and all five lignin types. The arithmetic means E^{r}_{μ} and H_{μ} and the standard deviations E^{r}_{σ} and H_{σ} are quantified from the remaining indents. The influence of the indent removal on the mean and standard deviation is further discussed in the Supplementary material Appendix B. The sought probability density functions for the indentation modulus $f(E^{\mathrm{r}})$ and for the hardness $f(H)$ (again specific for each indentation depth and each lignin type) are quantified using kernel density estimates (KDE) [47], as shortly described next. The KDE is a non-parametric approach to approximate the unknown probability density function of a dataset reading as [48,49]

$$f(x) = \frac{1}{nb}\sum_{i=1}^{n} K\left(\frac{x - x_i}{b}\right) \quad x \in \{E^{\mathrm{r}}, H\} \tag{2}$$

where n is the number of eligible indents, b is a smoothing parameter [48–50] labelled as bandwidth, x_i is the indent-specific indentation modulus E^{r}_i or hardness H_i, respectively, and $K(y)$ is the (non-negative) kernel function. We choose a Gaussian kernel distribution, as it is typically done [49], reading as

$$K(y) = \frac{1}{\sqrt{2\pi}} \exp\left(-\frac{1}{2}y^2\right). \tag{3}$$

The bandwidth b in Eqn 2 is estimated by a rule of thumb according to [51], reading as

$$b = 0.9 \min\left(x_{\sigma}, \frac{x_{\mathrm{IQR}}}{1.34}\right) n^{-1/5}, \tag{4}$$

where x_{σ} is the standard deviation and x_{IQR} the interquartile range of the indentation modulus and hardness, respectively.

Violin plots are used in the remainder of the paper to simultaneously depict the mean (red diamond point), standard deviation (red brackets), probability distribution functions (blue lines), and outliers (gray points) of modulus and hardness, see the example given in Fig. 1. Each considered indentation modulus or indentation hardness is thereby resembled by a blue point which is placed according to a Gauss distribution between the mirrored probability density functions.

3. Results and discussion

3.1. Porosity, mapping, and distance plots

First, the light microscopy images are discussed. The image analysis-based porosity of the five lignins is very different, it ranges from 6.5 % for K-SW to 56.2 % for OS-G, see the left column in Fig. 2 for low porosity lignin (E-HW, OS-HW, K-SW) and in Fig. 3 for high porosity lignin (OS-G, OS-SW). Additionally, for E-HW and OS-HW the bulk porosity is obtained based on specimen density measurements amounting to 1.17 g/cm^3 for E-HW and 1.12 g/cm^3 for OS-HW as well as the solid lignin density of 1.36 g/cm^3 [52]. The resulting bulk porosities of 14 % for E-HW and 18 % OS-HW agree well with the image analysis-based porosities indicating that the surface porosity is a good resemblance of the bulk porosity. The pore network is irregularly shaped but homogeneously distributed within the microstructure, except for the K-SW lignin, where regions with many pores are intermixed with pore-free regions. The characteristic pore dimensions range from 30 to 200 microns.

Next, indentation results are mapped on the microstructure images, see the right column in Figs. 2 and 3 for indentation modulus maps at indentation depths of 300 nm. As expected, large gradients of the modulus correlate well with the borders of the surface pores, and most of the indents located in surface pores exhibit smaller mechanical properties than indents which are located in lignin regions. In some areas outside the surface pores, similar significant stiffness gradients are observed, see e.g., Fig. 2f. This may indicate heterogeneity of the solid lignin itself, but likely also reveals locations with pores right below the surface.

To answer the question of whether the indents in the solid lignin areas characterize pure lignin or still "feel" the pores is tackled next. Therefore, the indentation modulus E^{r} is studied with respect to the boundary distance $d_{\min}$, see Fig. 4 for the realization of this plot for all indents with indentation depth of $h_{\max} = 300$ nm. Gray dots ($d_{\min} < 0$) and blue dots ($d_{\min} > 0$) refer to indentation points in pores and in lignin, respectively. To depict the trends, a moving average as well as a moving standard deviation (solid lines in Fig. 4) are included. Since the number of indents per indentation depth varies, the size of the truncated sliding window for the moving average and the standard deviation is chosen as 12 % of all the data points at this indentation depth, which provides an optimal smoothing for all indentation depths. The (average) indentation modulus increases with increasing distance to the pores. This shows that indents close to the pore-solid borders "feel" the surface pores and do not quantify the solid lignin itself. For the highly porous lignins labeled OS-SW and OS-G, the maximum distances $d_{\min}$ are rather small such that the indentation modulus never converges. For the less porous lignin, a plateau emerges after roughly 20 μm for E-HW, 70 μm for OS-HW, and 100 μm for K-SW. While

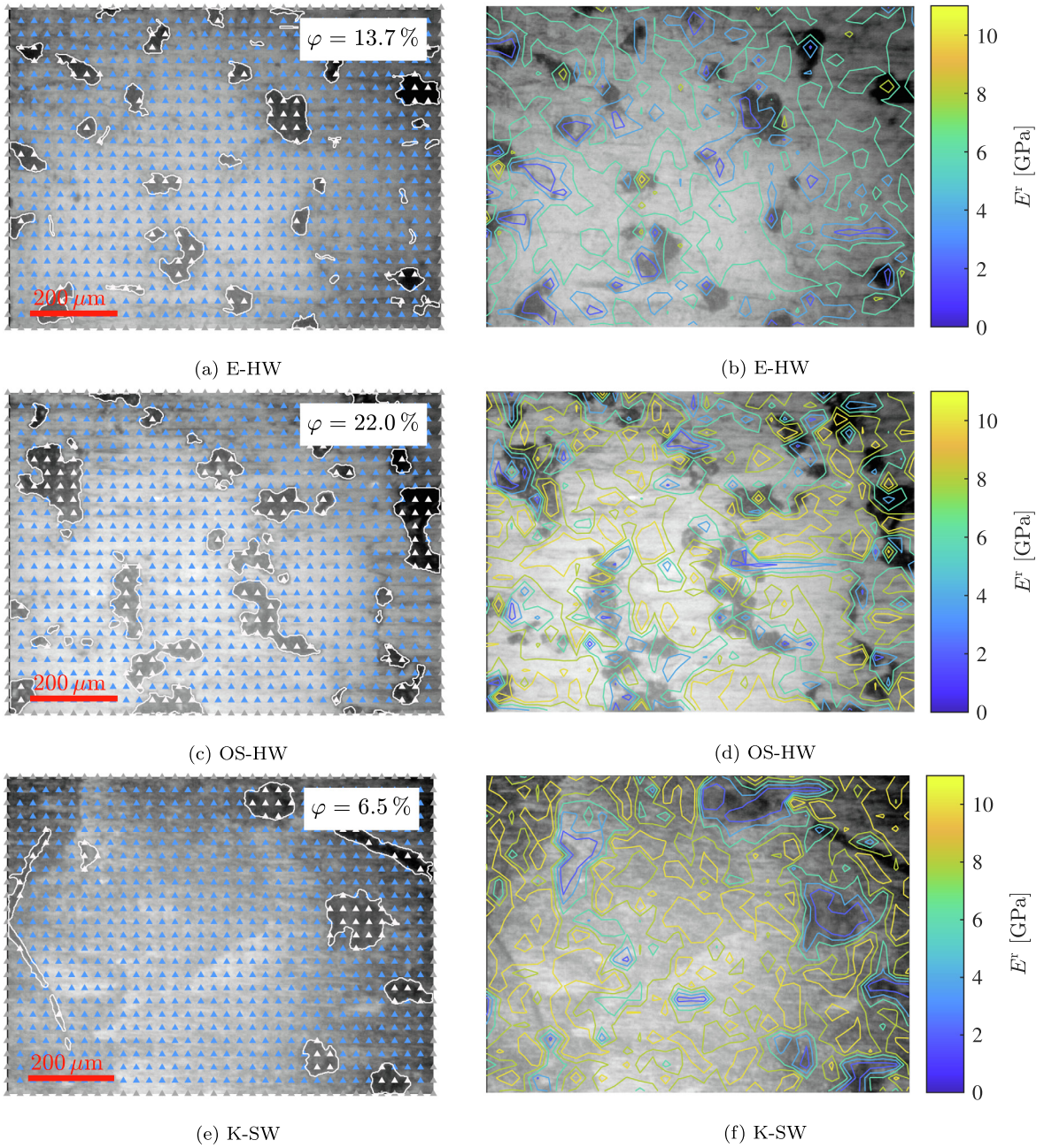

Fig. 2. Light microscopy image of the probed area (990 μm × 727 μm) of low-porous lignins at indentation depths of h_{max} = 300 nm: (a), (c), and (e) including the identified pores (dark gray areas with white borders) and a map of the indents in the pores (white triangles) as well as the indents used for evaluation (blue triangles); (b), (d), and (f) including a contour map of the indentation modulus E^r.

this indicates that the influence of the closest surface pore can be neglected for indents further away than this threshold, it still does not prove that these indents are not compromised by pores below the surface.

Better indicators, to judge whether the indents far away from the surface pores actually quantify pure lignin, or whether the indenter-probed volume still contains pores, are the scatter of the indentation moduli as well as the largest moduli. Given the solid-pore morphology and assuming a rather homogeneous solid lignin phase (we have no indication of heterogeneity), the scatter should decrease significantly, typically variation coefficients in other solid materials with our test setup are one order of magnitude smaller than achieved herein, see the evolution of indentation moduli with the boundary distance for a alkali-activated slag-fly ash mix tested by [45] as depicted in Fig. 4(f). Moreover, the largest measured moduli and hardness (or more precisely, a reasonable average of the largest few percent) should, theoretically speaking, refer to indents in a homogeneous half-space of solid lignin, given that any porosity would only soften the measured response. However, a significant number of indents reveal indentation properties that are significantly larger than the average plateaus values, unlike in our reference material in Fig. 4(f), where the plateau coincides with the *largest* measured values. This indicates that even though there is a convergence for our lignin samples, the plateau values do not refer to solid lignin. In other words, the majority of our indents characterize the lignin-pore composite rather than the solid lignin. Notably, the presented graphs in Fig. 4 refer to indentation depths of 300 nm, given the availability of large grids

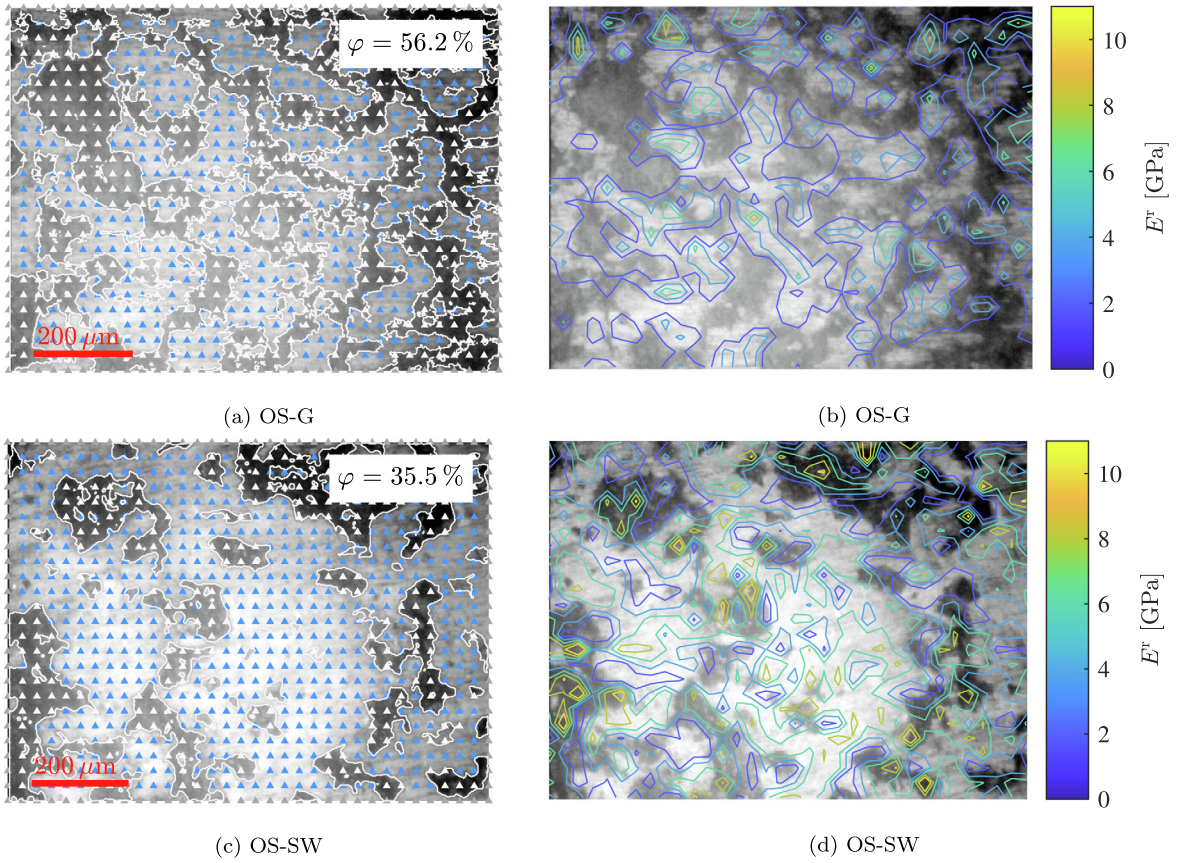

Fig. 3. Light microscopy image of the probed area (990 μm × 727 μm) of high-porous lignins at indentation depths of $h_{max} = 300$ nm: (a) and (c) including the identified pores (dark gray areas with white borders) and a map of the indents in the pores (white triangles) as well as the indents used for evaluation (blue triangles); (b) and (d) including a contour map of the indentation modulus E^r.

for all lignins at this indentation depth. The influence of pores is, obviously, even more pronounced for larger indentation depths, where indenter-probed volumes are larger, but even visible for indents with $h_{max} = 150$ nm. Before we further explore the influence of the pores, size effects are analyzed.

3.2. Indentation size effects and emerging of plateaus

Next, we discuss the influence of the indentation depth on the measured indentation moduli and hardnesses. The indentation properties decrease with increasing indentation depth, see Fig. 5 for the indentation modulus and Fig. 6 for the indentation hardness, whereby indents inside the surface porosity are excluded from now on. Such size effects are characteristic for indentation testing, and are studied mainly in the context of the hardness, but are also rather common for modulus testing, particularly but not exclusively for polymers [33,38,39,53–55]. As for the decrease of hardness with increasing indentation depth, several complementary explanations are discussed, e.g. the theory of shear transformation zones in polymers [38] and geometrically necessary dislocations in metals [35]. As for the modulus, the origin is less clear. The observed size effects are very likely the consequence of a combination of different individual contributions. First, the heterogeneity of the sample, particularly the contrast of mechanical properties between solid and pores may not only lead to an increased scatter at smaller indentation depths but also to increased mechanical properties [53]. Second, the indented surface may be altered [33], and may not be representative of the bulk material. Such surface effects may be related to material aging, most prominently to lignin oxidation. The modulus of oxidized lignin is up to two times larger than that of pure lignin, as recently revealed by the atomic force microscopy of lignin films [22]. A third contribution to the size effect may be related to the surface roughness. For the shallow intents at 150 nm depth, the ratio of contact depth to surface roughness, h_c/R_q, is close to the limit of roughly three, proposed by [41], which results in larger scatter as well as higher indentation properties [56]. It is remarkable that the indentation modulus and hardness only decrease until an indentation depth of 300 nm for E-HW and OS-SW and 600 nm for K-SW, OS-G, and OS-HW, respectively, see Figs. 5 and 6. At larger indentation depths, the average indentation properties remain virtually constant. The emerging plateaus demonstrate that it is possible to retrieve reliable size-independent indentation moduli of (porous) lignin by means of grid nanoindentation. This way, we define the reduced indentation moduli E^r_{pl} and the hardnesses H_{pl} as the average of all eligible indents (excluding the ones in surface pores as well as the statistical outliers) at indentation depths of 600 nm, 900 nm, and 1000 nm, see Tables 4 and 5. Notably, for all the lignins, except K-SW, even the 1200 nm deep indents coincide with the identified plateau values. As for the K-SW specimen, the damage might have occurred at 1200 nm deep indents, which might have led to the measured drop in mechanical properties.

Statistical analysis further reveals that the scatter in the indentation properties is smaller for indents at large indentation depths $h_{max} \geqslant 600$ nm compared to the shallow indents with $h_{max} \leqslant 300$ nm, comparing the corresponding probability density function and the markers for the standard deviation in the violin plots depicted in Figs. 5 and 6. Interestingly E-HW exhibits the smallest scatter and it is the lignin with the lowest porosity out

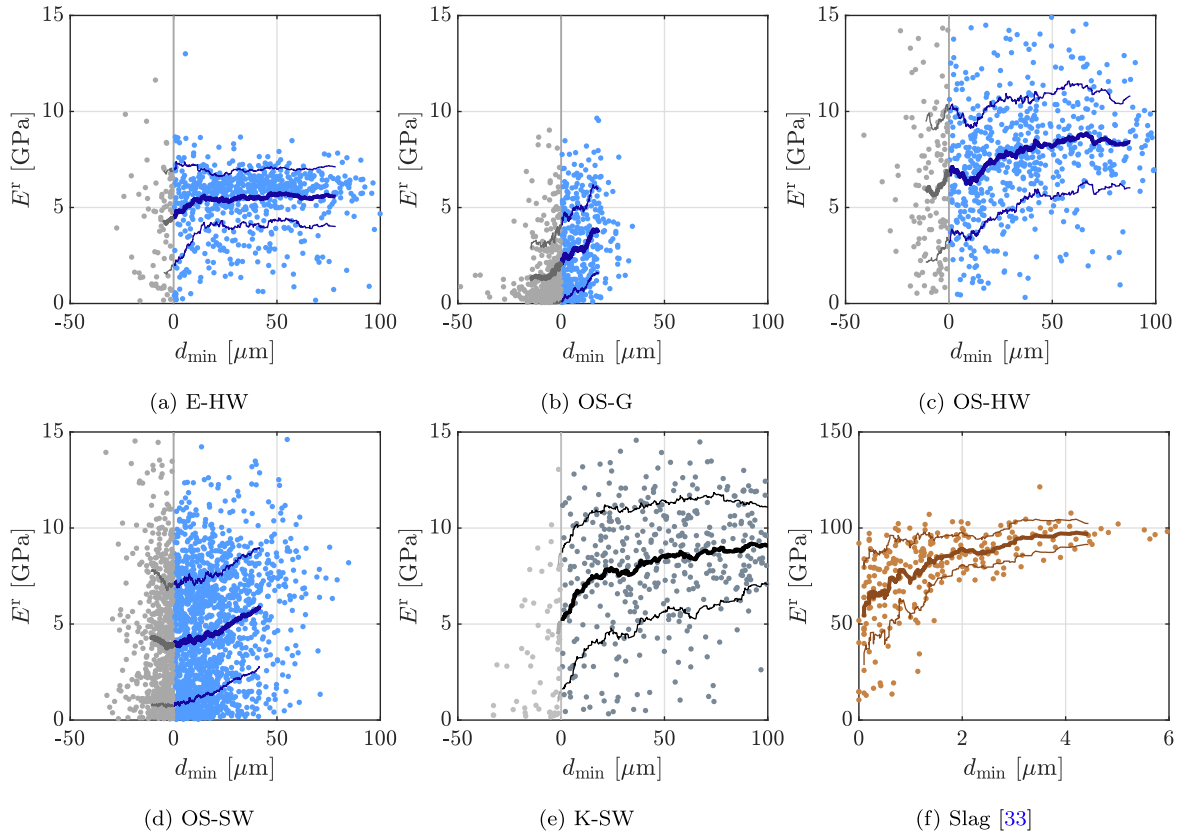

Fig. 4. Influence of minimum distance d_{min} between the pore border and the corresponding indent on the indentation modulus; gray points refer to indents in the surface pores, blue points to indents in lignin at maximum indentation depths of 300 nm, respectively; solid lines are the moving averages and standard deviations with a truncated sliding window containing 12 % of the total amount of points.

of the four lignins with high Klason lignin contents. The highest scatter is observed in the OS-G lignin, the lignin with the largest porosity. This trend suggests that the inhomogeneity due to the pores is most likely responsible for the scatter. The large scatter in K-SW lignin with low porosity can be attributed to the low Klason lignin content. Moreover, shallower indents, particularly in the highly porous lignins OS-G and OS-SW, have a less pronounced main peak. Even a second population at low stiffness emerges for OS-SW lignin. This results from a higher resolution of the indentation properties provided by the smaller indentation depth implying a smaller indenter-probed half-space, which is more likely located entirely in the solid region. K-SW has a reversed trend with a second population at high indentation depths, which might also be due to the low Klason lignin content.

3.3. From porous to solid lignin

From now on, we focus on the plateau data emerging at indentation depths of 600 to 1000 nm. First, we repeat the distance analyses and discuss the evolution of the respective indentation moduli as a function of the boundary distance d_{min}, see Fig. 7. Compared to the shallower indents shown in Fig. 4, there is no or only a small increase of the indentation modulus E^r with respect to increasing boundary distance d_{min}. Moreover, the moving averages agree, in good approximation, with the average indentation modulus at the plateau E^r_{plat} from the size-effect analysis. This corroborates that the deeper indents "feel", on average, most or all of the pores occurring in the composite. We, therefore, assume that the average indentation properties at the plateau, E^r_{pl} and H_{pl} characterize the (macroscopic) properties of *porous* lignin.

Next, we aim at back-identification of the mechanical properties of the solid lignin, E_{sl} and H_{sl}, from knowledge of the macroscopic properties of the porous lignin, E^r_{plat} and H_{plat}. Thus, the mechanical properties are first studied as a function of the measured porosity φ, see Fig. 8. The indentation properties decrease, as expected, with increasing porosity. Most remarkably, however, virtually unique master curves emerge, one for the modulus and one for the hardness.

To further explore the correlation between modulus and porosity, we adopt a micromechanics approach. Therefore, the porous lignin is considered as a representative volume element (RVE) consisting of two material phases, a solid lignin matrix and therein embedded spherical pores. To account for the matrix-inclusion morphology, see Figs. 2 and 3 the Mori–Tanaka [57,58] homogenization scheme is employed. This yields analytical functions for the homogenized Young's modulus E_{pl} and the homogenized Poisson's ratio ν_{pl} of the porous lignin as a function of the (measured) porosity φ, reading as

$$E_{pl} = \frac{2E_{sl}\,(5\nu_{sl}-7)\,(1-\varphi)}{15\nu_{sl}^2\varphi + 2\nu_{sl}\,(5+\varphi) - 13\varphi - 14}, \quad (5)$$

$$\nu_{pl} = \frac{5\nu_{sl}^2\,(2+\varphi) + 2\nu_{sl}\,(-7+\varphi) - 3\varphi}{15\nu_{sl}^2\varphi + 2\nu_{sl}\,(5+\varphi) - 13\varphi - 14}, \quad (6)$$

where E_{sl} is Young's modulus and ν_{sl} is Poisson's ratio of solid lignin. The latter cannot be evaluated with nanoindentation and is, to our knowledge, not reported in the literature. Therefore, the Poisson's ratio of solid lignin is assumed based on typical Poisson's ratios for polymers [59], as $\nu_{sl} = 0.4$. To investigate the influence of the Poisson's ratio on the solid and porous Young's modulus, additional ν_{sl} of 0.3 and 0.5 are considered, as discussed later. The Young's

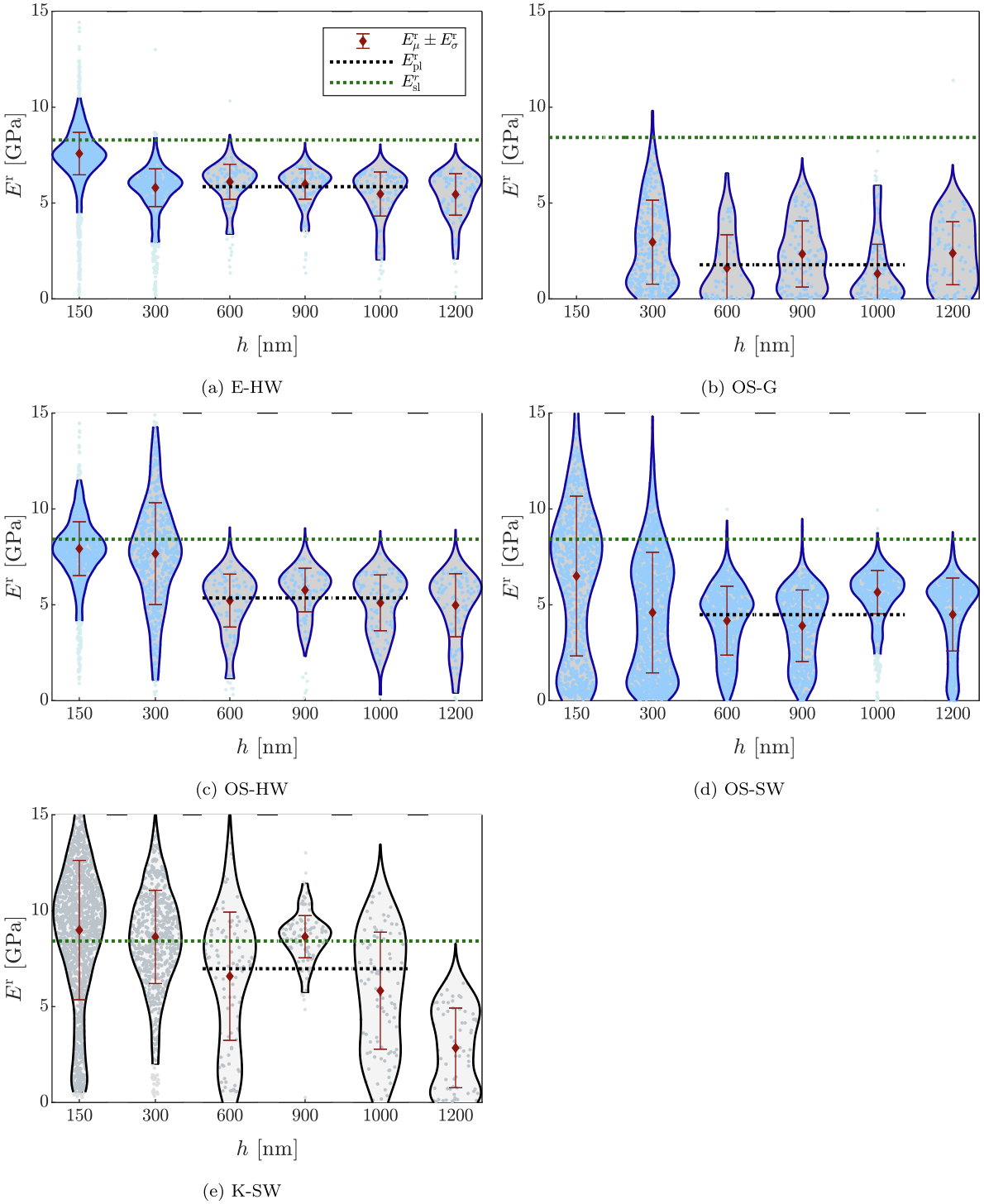

Fig. 5. Violin plots of the indentation modulus E^r with mean modulus E^r_μ, standard deviation E^r_σ, plateau modulus E^r_{pl}, and solid lignin modulus E^r_{sl} according to Fig. 8.

modulus of the porous lignin E_{pl} is calculated from the measured indentation modulus E^r_{pl} according to Eq. (1). Motivated by the strong correlation revealed by Fig. 8a, we consider that the solid lignin in all five tested lignin-pore composites is mechanically identical, i.e. we assume that solid lignin – irrespective of its origin and extraction process – exhibits an intrinsic stiffness. The sought Young's modulus of solid lignin E_{sl} is obtained by fitting, in more detail, by minimizing the error between the homogenized and nanoindentation-derived Young's moduli of the four tested porous lignins with high Klason lignin content (E-HW, OS-G, OS-HW, and OS-SW). This results in an intrinsic Young's modulus of $E_{sl} = 7.12$ GPa, which can be translated into a corresponding reduced indentation modulus of $E^r_{sl} = 8.42$ GPa by applying Eq. (1). The Mori–Tanaka modeling results reproduce the measured trend of indentation modulus E^r_{pl} vs. porosity φ very well, see Fig. 8a, indicated by coefficients of determination $R^2 = 91\%$. This excellent agreement corroborates the hypothesis that the stiffness difference in the four tested lignin materials is mainly attributed to the difference in porosity, and that the stiffness of the solid lignin

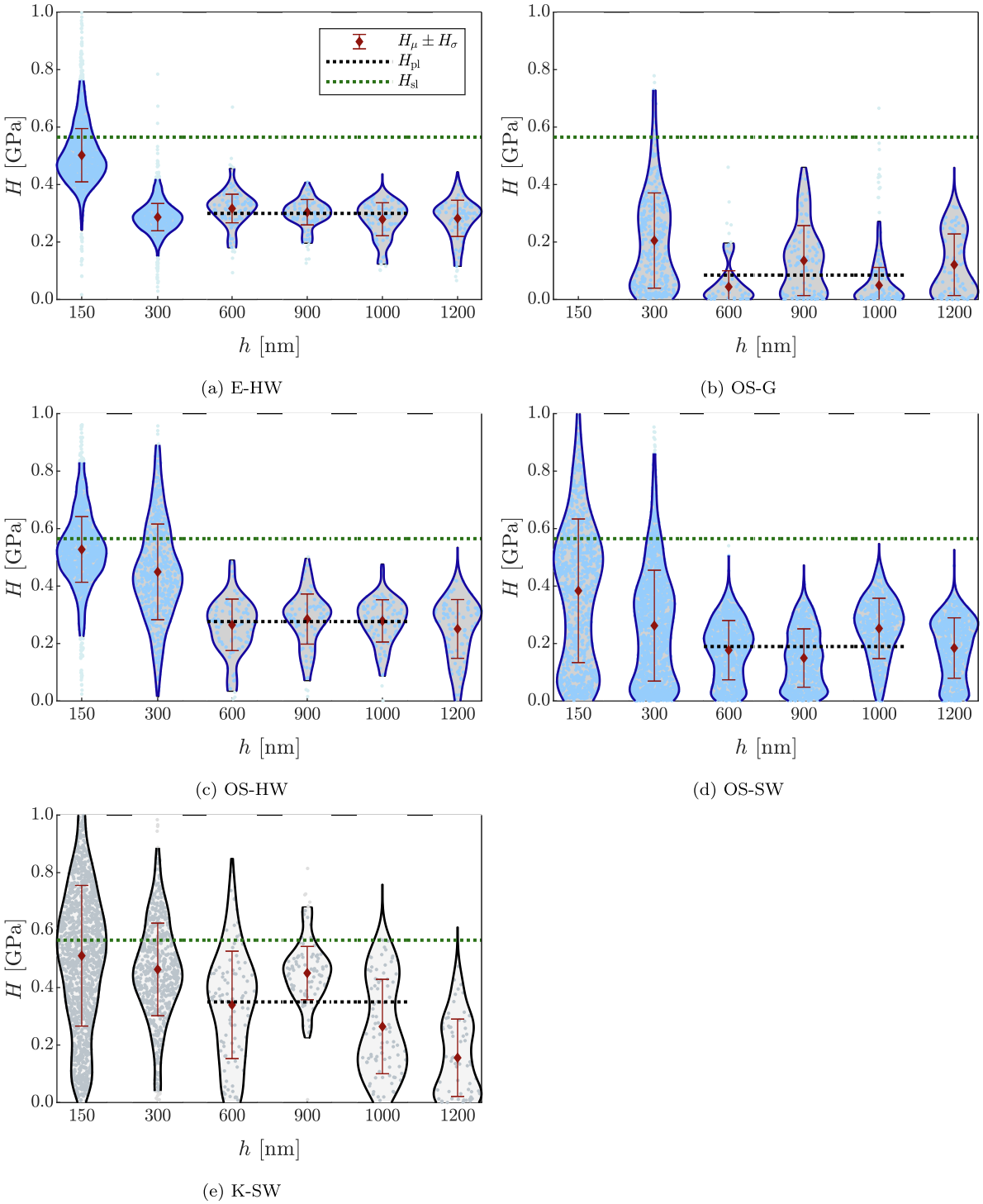

Fig. 6. Violin plots of the indentation hardness H with mean hardness H_μ, standard deviation H_σ, plateau hardness H_{pl}, and solid lignin hardness H_{sl} according to Fig. 8.

Table 4
Indentation modulus E^r (mean ± standard deviation) for each depth h_{max} and plateau values (h_{max} = 600 to 1000 nm).

	E^r [GPa]						
h_{max} [nm]	150	300	600	900	1000	1200	plateau
E-HW	7.58 ± 1.11	5.80 ± 0.99	6.11 ± 0.92	5.98 ± 0.79	5.47 ± 1.15	5.45 ± 1.08	5.85 ± 1.00
OS-G		2.96 ± 2.19	1.61 ± 1.73	2.34 ± 1.73	1.31 ± 1.54	2.38 ± 1.64	1.78 ± 1.71
OS-HW	7.93 ± 1.40	7.67 ± 2.66	5.22 ± 1.38	5.77 ± 1.14	5.10 ± 1.46	4.98 ± 1.64	5.36 ± 1.36
OS-SW	6.50 ± 4.17	4.59 ± 3.14	4.17 ± 1.80	3.90 ± 1.87	5.66 ± 1.13	4.49 ± 1.90	4.48 ± 1.82
K-SW	8.99 ± 3.63	8.63 ± 2.43	6.58 ± 3.35	8.65 ± 1.10	5.83 ± 3.05	2.85 ± 2.08	6.98 ± 2.96

Table 5
Indentation hardness H (mean ± standard deviation) for each depth h_{max} and plateau values (h_{max} = 600 to 1000 nm).

	H [MPa]						
h_{max} [nm]	150	300	600	900	1000	1200	plateau
E-HW	0.502 ± 0.093	0.287 ± 0.048	0.317 ± 0.050	0.304 ± 0.044	0.279 ± 0.057	0.282 ± 0.063	0.300 ± 0.053
OS-G		0.205 ± 0.166	0.044 ± 0.056	0.135 ± 0.122	0.049 ± 0.062	0.121 ± 0.107	0.085 ± 0.101
OS-HW	0.528 ± 0.114	0.449 ± 0.166	0.265 ± 0.090	0.285 ± 0.087	0.279 ± 0.074	0.251 ± 0.102	0.276 ± 0.084
OS-SW	0.384 ± 0.250	0.262 ± 0.193	0.177 ± 0.103	0.150 ± 0.102	0.253 ± 0.105	0.184 ± 0.105	0.190 ± 0.111
K-SW	0.511 ± 0.245	0.463 ± 0.161	0.340 ± 0.187	0.450 ± 0.093	0.264 ± 0.164	0.156 ± 0.135	0.350 ± 0.172

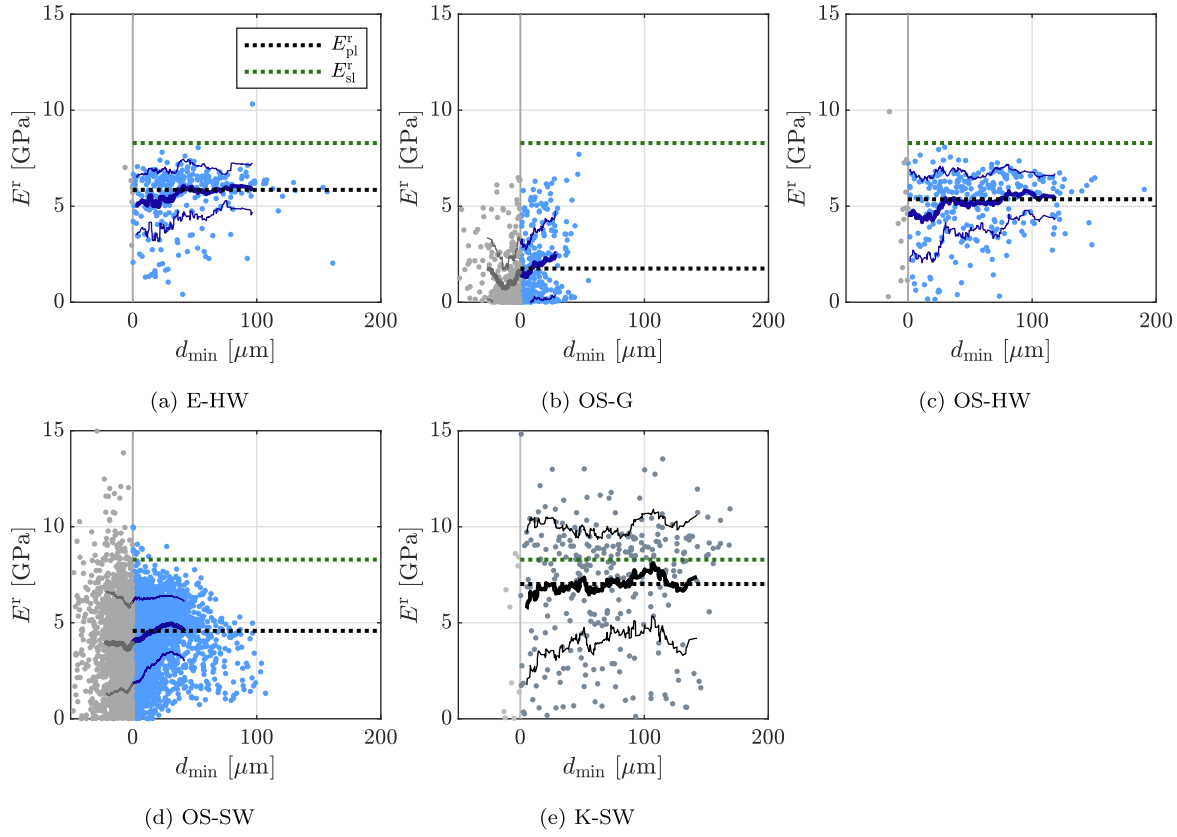

Fig. 7. Influence of minimum distance d_{min} between the pore border and the corresponding indent on the indentation modulus; gray points refer to indents in the surface pores, blue points to indents in lignin at the plateau (h_{max} = 600 to 1000 nm), respectively; solid lines are the moving averages and standard deviations with a truncated sliding window containing 12 % of the total amount of points.

is, in good approximation, identical. Even the low Klason lignin K-SW nicely follows the trend of the other four lignins.

The Poisson's ratio only slightly influences the indentation modulus predicted by the micromechanics model. The indentation modulus for solid lignin ranges from 8.67 GPa to 8.24 GPa for Poisson's ratios form 0.5 to 0.3, which is a typical range for polymers [59]. This discrepancy even decreases with increasing porosity, see Fig. 8a. The conversion of the indentation modulus to the Young's modulus is Poisson's ratio sensitive and results in a Young's modulus of 6.55 GPa and 7.55 GPa for Poisson's ratios of 0.5 and 0.3, respectively.

Similar to the Young's modulus, we assume that solid lignin exhibits intrinsic strength properties, which can be retrieved from hardness–packing density scaling relations for cohesive-frictional porous materials according to [60]. This way, the hardness of porous lignin can be expressed as a function of the porosity φ and of the cohesion of solid lignin c_{sl} employing a Mori–Tanaka homogenization scheme and a Von-Mises failure criterion, as

$$H_{pl} = 12c_{sl}(1-\varphi)\frac{a - b(1-\varphi)}{(23 - c(1-\varphi))\sqrt{8 - 5(1-\varphi)}}, \tag{7}$$

where $a = 7.0$, $b = 3.721366$, and $c = 18.39049$ are constants associated with the Mori Tanaka homogenization and the Berkovich indenter geometry [60]. The cohesion of solid lignin is gained by minimizing the error between the hardness–packing density scaling relation and the nanoindentation-derived hardness of E-HW, OS-HW, OS-SW, and OS-G, resulting in $c_{sl} = 0.115$ GPa. Evaluating Eq. (7) for $\varphi = 0$ and $c_{sl} = 0.115$ GPa results in the solid lignin hardness of $H_{sl} = 0.565$ GPa. By analogy to the stiffness, nanoindentation suggests that the hardness and cohesion of the solid lignin in all five samples is virtually identical.

Finally, we compare the back-identified properties of solid lignin with the results of the individual indents. The identified solid lignin properties act, except for K-SW lignin, as an upper bound for the indentation properties measured with $h_{max} = \{600, 900, 1000\,\text{nm}\}$, see Figs. 5–7. This corroborates that most indenter-probed volumes contain some porosity, and that the indentation properties thus characterize porous lignin. Only

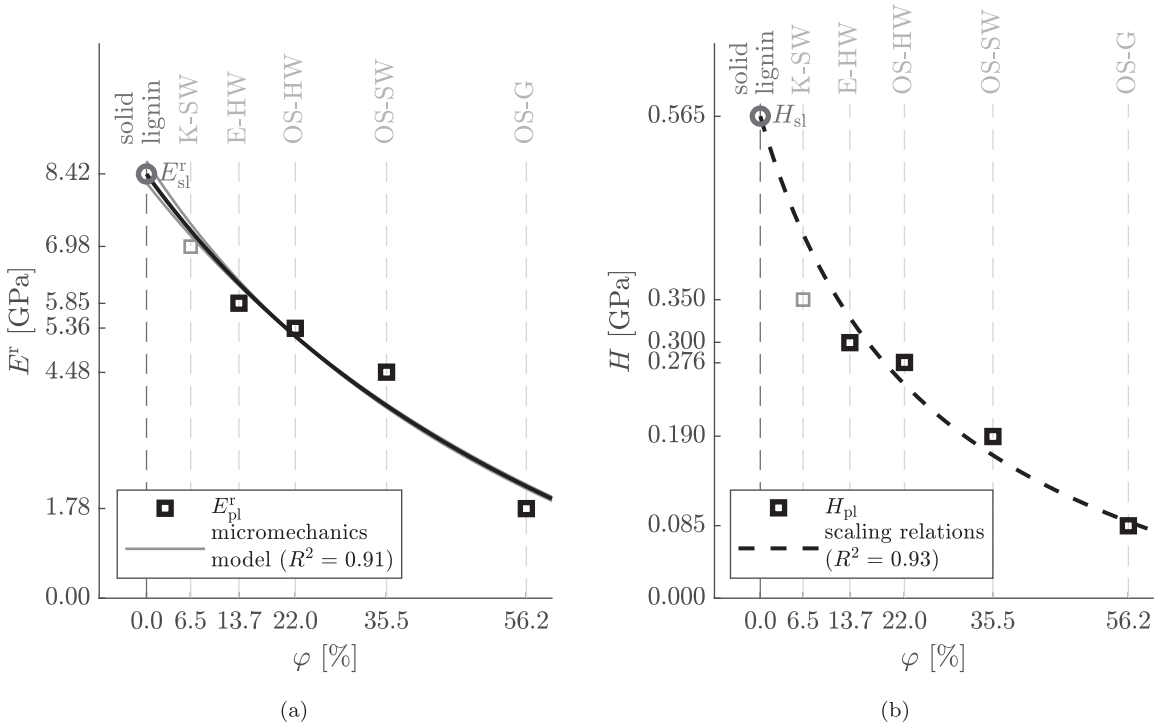

Fig. 8. Porosity-dependent indentation properties of porous and solid lignin: (a) nanoindentation-derived plateau moduli E^r_{pl} (square points) compared to best-fit Mori–Tanaka homogenization results (black line: $\nu_{sl} = 0.4$; gray lines: $\nu_{sl} = \{0.3, 0.5\}$), which predict, at zero porosity the indentation modulus of solid lignin E^r_{sl}, (b) nanoindentation-derived plateau hardness H_{pl} with a fit of the scaling relations according to [60] predicting the solid lignin hardness H_{sl} at 0 % porosity.

if the probed half-space is free of pores, and thus only for a very small quantity of the many thousand individual indents, solid lignin is indented and the corresponding mechanical indentation properties thus match the solid lignin properties. At shallower depths, a few indents exhibit unreasonably high indentation properties, a size effect discussed in Section 3.2 in more detail. As for K-SW specimen, the low Klason-lignin content might indicate that the solid matrix is heterogeneous, a hypothesis that would explain the relatively large scatter and that measured modulus/hardness results exceed the solid lignin properties. Nevertheless, the plateau value of K-SW lignin agrees well with the micromechanics fit.

3.4. Comparison to stiffness data from literature

The identified Young's modulus of solid lignin agrees with the Young's modulus of the alkali lignin particle identified by [21] using atomic force microscopy and tested at roughly the same relative humidity of 35 %. The reported Young's moduli of 7.1 GPa [24], 6.9 GPa [25], and 7.5 GPa [26], obtained from nanoindentation in the lignin-rich middle lamella of softwood cells, also agree very well with the herein identified Youngs modulus. The indentation hardnesses from the middle lamella of 0.43 GPa [24] and 0.42 GPa [26] are slightly lower than the herein estimated solid lignin hardness, which might be explained by differences in the chemistry and porosity between the hot-pressed lignins and the lignin naturally occurring in the middle lamella, or by nanoindentation strain rate effects discussed in the next subsection. We may conclude that neither extraction processes, nor hot-pressing of lignin does change its mechanical properties significantly. Moreover, the fact that we obtain the same stiffness for our (solid) lignin matrix in the hot-pressed samples as [21] for (unpressed) lignin particles indicates that hot-pressing at 108 MPa and 90 °C for 2 min (see Section 2.1) results in a defect-free matrix, albeit with potentially significant porosity.

3.5. Influence of viscoelasticity and strain rate

The very significant decrease of the force during the holding phase (see typical force–displacement diagram depicted in Fig. 9) highlights the viscoelastic nature of the tested lignin samples. Indentation in viscoelastic materials is challenging, as the viscous response, i.e. creep and relaxation, might alter the indentation properties [61–63]. Herein, we discuss potential dependencies of the obtained mechanical properties on (i) the viscoelastic nature of the material and (ii) the strain rate. To minimize the influence, the indentation test campaign was designed with a five-second-long force plateau and a rather slow loading. This way, a large part of the viscoelastic strains can decay already before the unloading starts. The absence of a "nose" in the unloading curves [61,63] is one indicator that viscoelastic effects may be negligible. More quantitatively, all our individual indents fulfill the criterion that the unloading (force) rate $\dot{P}$ at the beginning of unloading is at least 30 times larger than the one at the end of the holding phase, an empirical criterion established by [64] for indentation creep tests. Even more evidence for a negligible influence of creep on the measured elastic modulus can be obtained when adopting the modulus correction developed by [62] to our relaxation tests. This results in an increase of the indentation modulus by only 3 % on average, and it is therefore omitted in the main part of the paper. The measured hardness may be influenced by relaxation [65]. Quantitive ways for correcting the hardness in relaxation tests are not found in the literature. It is, however, very likely that viscosity affects the hardness of the different lignins to a similar extent. This way, the obtained hardnesses relative to each other, and thus also the revealed correlation of hardness vs. porosity are still valid, while the absolute values may indeed be different.

Next, strain rate dependencies are discussed. Polymer indentation testing reveals that the indentation modulus remains constant with respect to changes in the loading/unloading strain rate [38].

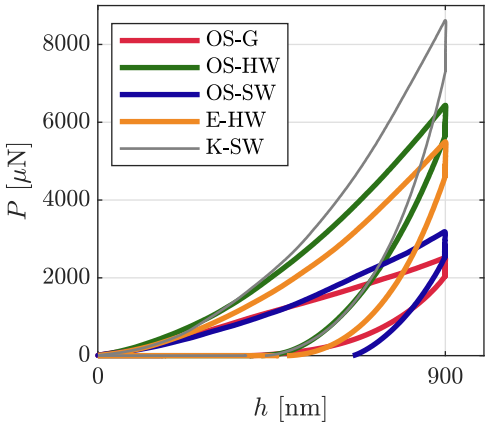

Fig. 9. Force–displacement (P-h) curves of the five tested lignins; whereby out of the 20650 recorded individual P-h curves, five representative ones are depicted for which the individual indentation modulus is close to the average indentation modulus at an indentation depth of 900 nm.

The hardness of polymers, in turn, is significantly influenced by the strain rate of the loading and unloading phase [38,66]. Exploiting the similarity of lignin and typical polymers, similar dependencies might be expected for our tested lignins. We note that the employed load history in all our displacement-controlled indentation tests is similar, consisting of ten seconds of loading, five seconds of holding the load constant, and ten seconds of unloading. Moreover, the average strain rates $\dot{h}/h$ are equivalent for all indentation depths, and amount to 0.1 s^{-1} at the end of loading and the beginning of the unloading phase. This way, any strain rate effects would, most likely, concern all lignins similarly, and would thus not change the main conclusions of our work. This discussion, however, clearly highlights that the absolute hardness results should be treated with caution, and provides lots of motivation for future work.

4. Conclusion

20650 nanoindentation tests at maximum indentation depths ranging from 150 nm to 1200 nm are performed on five different lignin samples, obtained from hot-pressing five different technical lignins. The indents in the (production-related) pores were excluded using image segmentation of light microscopy images. The remaining indents were statistically evaluated, which led to the following findings:

1. Reliable mechanical properties of lignin can be retrieved with light microscopy-aided grid nanoindentation by excluding the indents in the surface pores and by considering indentation depths between 600 nm and 1000 nm where surface effects vanish. The resulting indentation moduli range from 1.8 GPa to 7.0 GPa, the hardness, in turn, ranges from 0.09 GPa to 0.40 GPa, depending on the lignin sample.
2. Indentation properties however are strongly correlated with sample porosities, suggesting that almost all indents "feel" the pores, and thus characterize a *porous* lignin composite.
3. The stiffness of *solid* lignin, back-identified from micromechanics-based Mori–Tanaka homogenization, is however, virtually constant for all five tested lignins, quantified by indentation moduli of 8.4 GPa or Young's moduli of 7.1 GPa. The hardness of *solid* lignin, back-identified from hardness–packing density scaling relations [60], is constant as well and amounts to 0.57 GPa, but this absolute value may be affected by the viscous nature of the material or the strain rate. This underlines that the herein studied lignins, from both different extraction processes (Kraft pulping, organosolv, enzymatic hydrolysis) and different feedstocks (softwood, hardwood, grass), are mechanically rather similar.

Data availability

Data will be made available on request.

Declaration of Competing Interest

The authors declare that they have no known competing financial interests or personal relationships that could have appeared to influence the work reported in this paper.

Acknowledgements

The funding from the Austrian Science Fund (FWF) through the START grant Y1093 "Virtual Wood Labs" and SFB F77 "Advanced Computational Design" is gratefully acknowledged.

Appendix A. OS-SW extraction

OS-SW lignin was produced following a standard organosolv extraction procedure [67,68]. Spruce sawdust milled to 1 mm and 60 wt.% aqueous ethanol were heated up to 180 and 220 °C in a 1 L stirred autoclave (Zirbus, HAD 9/16, Bad Grund, Germany). The resulting extracts from each heating process were mixed together and first rotavapored at 50 °C and 60 mbar, and then freeze-dried to remove the solvent. Then, the sample was mixed with water, vortexed, and centrifuged at 15000 rpm for 20 min. The supernatant was discarded, fresh water was added and the procedure was repeated three times. The final washed solid was freeze-dried to obtain a solid lignin powder.

Appendix B. Supplementary material

Supplementary data associated with this article can be found, in the online version, at https://doi.org/10.1016/j.matdes.2023.111765.

References

[1] E. Windeisen, G. Wegener, Lignin as building unit for polymers, Polymer Science: A Comprehensive Reference, 10 Volume Set, vol. 10, Elsevier, 2012, ISBN 9780080878621, pp. 255–265, https://doi.org/10.1016/B978-0-444-53349-4.00263-6.
[2] S. Haghdan, S. Renneckar, G.D. Smith, Sources of lignin, in: O. Faruk, M. Sain (Eds.), Lignin in Polymer Composites, William Andrew Publishing, 2016, ISBN 978-0-323-35565-0, pp. 1–11, https://doi.org/10.1016/B978-0-323-35565-0.00001-1.
[3] A. Khan, V. Nair, J.C. Colmenares, R. Gläser, Lignin-based composite materials for photocatalysis and photovoltaics, Top. Curr. Chem., 2364-8961 376 (3) (2018) 1–31, https://doi.org/10.1007/S41061-018-0198-Z.
[4] J. Huang, S. Fu, L. Gan, Chapter 4 - lignin chemicals and their applications, in: Lignin Chemistry and Applications, Elsevier, 2019, ISBN 978-0-12-813941-7, pp. 79–134, https://doi.org/10.1016/B978-0-12-813941-7.00004-7.
[5] Y. Matsushita, Conversion of technical lignins to functional materials with retained polymeric properties, J. Wood Sci., 14350211 61 (3) (2015) 230–250, https://doi.org/10.1007/s10086-015-1470-2.
[6] E.K. Pye, Industrial Lignin Production and Applications, vol. 2, John Wiley & Sons Ltd., 2008, ISBN 9783527619849, pp. 165–200, https://doi.org/10.1002/9783527619849.ch22. Chapter 5.
[7] M.M. Abu-Omar, K. Barta, G.T. Beckham, J.S. Luterbacher, J. Ralph, R. Rinaldi, Y. Román-Leshkov, J.S. Samec, B.F. Sels, F. Wang, Guidelines for performing lignin-first biorefining, Energy Environ. Sci., 1754-5706 14 (1) (2021) 262–292, https://doi.org/10.1039/D0EE02870C.
[8] A. Yuliestyan, M. García-Morales, E. Moreno, V. Carrera, P. Partal, Assessment of modified lignin cationic emulsifier for bitumen emulsions used in road paving, Mater. Des., 0264-1275 131 (2017) 242–251, https://doi.org/10.1016/j.matdes.2017.06.024.

[9] Q. Yan, R. Arango, J. Li, Z. Cai, Fabrication and characterization of carbon foams using 100 % kraft lignin, Mater. Des., 0264-1275 201 (2021) 109460, https://doi.org/10.1016/j.matdes.2021.109460.

[10] K. Kaewtatip, J. Thongmee, Effect of kraft lignin and esterified lignin on the properties of thermoplastic starch, Mater. Des., 0261-3069 49 (2013) 701–704, https://doi.org/10.1016/j.matdes.2013.02.010.

[11] H. Abdul Khalil, M. Marliana, A. Issam, I. Bakare, Exploring isolated lignin material from oil palm biomass waste in green composites, Mater. Des., 0261-3069 32 (5) (2011) 2604–2610, https://doi.org/10.1016/j.matdes.2011.01.035.

[12] E. Pregi, D. Kun, G. Faludi, J. Móczó, B. Pukánszky, Modeling the mechanical properties of polypropylene/lignin/flax hybrid composites, Mater. Des., 0264-1275 220 (2022) 110833, https://doi.org/10.1016/j.matdes.2022.110833.

[13] R. Sailaja, M. Deepthi, Mechanical and thermal properties of compatibilized composites of polyethylene and esterified lignin, Mater. Des., 0261-3069 31 (9) (2010) 4369–4379, https://doi.org/10.1016/j.matdes.2010.03.046.

[14] Y. Ge, L. Qin, Z. Li, Lignin microspheres: An effective and recyclable natural polymer-based adsorbent for lead ion removal, Mater. Des., 0264-1275 95 (2016) 141–147, https://doi.org/10.1016/j.matdes.2016.01.102.

[15] A. García, A. Toledano, M. Ángeles Andrés, J. Labidi, Study of the antioxidant capacity of miscanthus sinensis lignins, Process Biochem., 1359-5113 45 (6) (2010) 935–940, https://doi.org/10.1016/j.procbio.2010.02.015.

[16] A. Eraghi Kazzaz, P. Fatehi, Technical lignin and its potential modification routes: A mini-review, Ind. Crops Prod., 0926-6690 154 (2020) 112732, https://doi.org/10.1016/j.indcrop.2020.112732.

[17] F.S. Chakar, A.J. Ragauskas, Review of current and future softwood kraft lignin process chemistry, Ind. Crops Prod., 0926-6690 20 (2) (2004) 131–141, https://doi.org/10.1016/j.indcrop.2004.04.016. 6th International Lignin Institute conference.

[18] W.J. Cousins, R.W. Armstrong, W.H. Robinson, Young's modulus of lignin from a continuous indentation test, J. Mater. Sci., 1573-4803 10 (10) (1975) 1655–1658, https://doi.org/10.1007/BF00554925.

[19] W.J. Cousins, Elasticity of isolated lignin: Young's modulus by a continuous indentation method, N. Z. J. For. Sci. 7 (1) (1977) 107–112.

[20] W.J. Cousins, Elastic modulus of lignin as related to moisture content, Wood Sci. Technol. 10 (1) (1976) 9–17.

[21] K.M. Hess, J.P. Killgore, W.V. Srubar, Nanoscale hygromechanical behavior of lignin, Cellulose, 1572882X 25 (11) (Nov 2018) 6345–6360, https://doi.org/10.1007/S10570-018-2045-3.

[22] C. Marcuello, L. Foulon, B. Chabbert, V. Aguié-Béghin, M. Molinari, Atomic force microscopy reveals how relative humidity impacts the Young's modulus of lignocellulosic polymers and their adhesion with cellulose nanocrystals at the nanoscale, Int. J. Biol. Macromol., 0141-8130 147 (2020) 1064–1075, https://doi.org/10.1016/J.IJBIOMAC.2019.10.074.

[23] A. Manisekaran, P. Grysan, B. Duez, D.F. Schmidt, D. Lenoble, J.-S. Thomann, Solvents drive self-assembly mechanisms and inherent properties of Kraft lignin nanoparticles (<50 nm), J. Colloid Interface Sci., 0021-9797 626 (2022) 178–192, https://doi.org/10.1016/J.JCIS.2022.06.089.

[24] L. Wagner, T.K. Bader, K. De Borst, Nanoindentation of wood cell walls: Effects of sample preparation and indentation protocol, J. Mater. Sci., 00222461 49 (1) (2014) 94–102, https://doi.org/10.1007/s10853-013-7680-3.

[25] R. Wimmer, B.N. Lucas, Comparing mechanical properties of secondary wall and cell corner middle lamella in spruce wood, IAWA J., 0928-1541 18 (1) (1997) 77–88, https://doi.org/10.1163/22941932-90001463.

[26] W. Gindl, H.S. Gupta, T. Schöberl, H.C. Lichtenegger, P. Fratzl, Mechanical properties of spruce wood cell walls by nanoindentation, Appl. Phys. A, 1432-0630 79 (8) (2004) 2069–2073, https://doi.org/10.1007/S00339-004-2864-Y.

[27] S. Youssefian, N. Rahbar, Molecular origin of strength and stiffness in bamboo fibrils, Sci. Rep., 20452322 5 (2015) 1–13, https://doi.org/10.1038/srep11116.

[28] S. Youssefian, J.E. Jakes, N. Rahbar, Variation of Nanostructures, Molecular Interactions, and Anisotropic Elastic Moduli of Lignocellulosic Cell Walls with Moisture, Sci. Rep., 2045-2322 7 (1) (2017) 1–10, https://doi.org/10.1038/s41598-017-02288-w.

[29] C. Zhang, K. Kulasinski, D. Derome, J. Carmeliet, Coupled Hygro-Thermo-Mechanical Behavior of Amorphous Biopolymers: Molecular Dynamic Study of Softwood Lignin, in: Poromechanics 2017 - Proceedings of the 6th Biot Conference on Poromechanics, 2017, pp. 809–814. doi:10.1061/9780784480779.100.

[30] C. Zhang, M. Chen, S. Keten, B. Coasne, D. Derome, J. Carmeliet, Hygromechanical mechanisms of wood cell wall revealed by molecular modeling and mixture rule analysis, Sci. Adv. 7 (37) (2021), https://doi.org/10.1126/sciadv.abi8919.

[31] G. Constantinides, K.S. Ravi Chandran, F.J. Ulm, K.J. Van Vliet, Grid indentation analysis of composite microstructure and mechanics: Principles and validation, Mater. Sci. Eng.: A, 0921-5093 430 (1–2) (2006) 189–202, https://doi.org/10.1016/J.MSEA.2006.05.125.

[32] W. Oliver, G. Pharr, An improved technique for determining hardness and elastic modulus using load and displacement sensing indentation experiments, J. Mater. Res. 7 (6) (1992) 1564–1583, https://doi.org/10.1557/JMR.1992.1564.

[33] C.A. Charitidis, Nanoscale deformation and nanomechanical properties of polydimethylsiloxane (PDMS), Ind. Eng. Chem. Res. 50 (2) (2011) 565–570, https://doi.org/10.1021/ie100099g.

[34] L. Shen, T. Liu, P. Lv, Polishing effect on nanoindentation behavior of nylon 66 and its nanocomposites, Polym. Testing, 0142-9418 24 (6) (2005) 746–749, https://doi.org/10.1016/j.polymertesting.2005.04.004.

[35] W.D. Nix, H. Gao, Indentation size effects in crystalline materials: A law for strain gradient plasticity, J. Mech. Phys. Solids, 00225096 46 (3) (1998) 411–425, https://doi.org/10.1016/S0022-5096(97)00086-0.

[36] G.M. Pharr, E.G. Herbert, Y. Gao, The indentation size effect: A critical examination of experimental observations and mechanistic interpretations, Annu. Rev. Mater. Res., 15317331 40 (2010) 271–292, https://doi.org/10.1146/annurev-matsci-070909-104456.

[37] A. Sluiter, B. Hames, R. Ruiz, C. Scarlata, J. Sluiter, D. Templeton, Technical Report NREL/TP-510-42618: Determination of Structural Carbohydrates and Lignin in Biomass, Technical report, National Renewable Energy Laboratory, Golden, Colorado, 2012.

[38] G.Z. Voyiadjis, L. Malekmotiei, A. Samadi-Dooki, Indentation size effect in amorphous polymers based on shear transformation mediated plasticity, Polymer, 0032-3861 137 (2018) 72–81, https://doi.org/10.1016/j.polymer.2018.01.006.

[39] C.S. Han, S.H. Sanei, F. Alisafaei, On the origin of indentation size effects and depth dependent mechanical properties of elastic polymers, J. Polym. Eng., 03346447 36 (1) (2016) 103–111, https://doi.org/10.1515/polyeng-2015-0030.

[40] Y.Y. Lim, M. Munawar Chaudhri, Indentation of elastic solids with a rigid vickers pyramidal indenter, Mech. Mater., 0167-6636 38 (12) (2006) 1213–1228, https://doi.org/10.1016/j.mechmat.2006.04.006.

[41] E. Donnelly, S.P. Baker, A.L. Boskey, M.C. Van Der Meulen, Effects of surface roughness and maximum load on the mechanical properties of cancellous bone measured by nanoindentation, J. Biomed. Mater. Res. - Part A, 15493296 77 (2) (2006) 426–435, https://doi.org/10.1002/jbm.a.30633.

[42] D. Bradley, G. Roth, Adaptive thresholding using the integral image, J. Graph. Tools 12 (2) (2007) 13–21, https://doi.org/10.1080/2151237X.2007.10129236.

[43] J.A. Sethian, Level set methods and fast marching methods: Evolving interfaces in computational geometry, fluid mechanics, computer vision, and materials science, 2. edition., Cambridge monographs on applied and computational mathematics. Cambridge Univ. Press, Cambridge, 1999, ISBN 0521642043.

[44] MATLAB, version 9.12.0 (R2022a), The MathWorks Inc., Natick, Massachusetts, 2022.

[45] M. Königsberger, L. Zelaya-Lainez, O. Lahayne, B.L. Pichler, C. Hellmich, Nanoindentation-probed Oliver-Pharr half-spaces in alkali-activated slag-fly ash pastes: Multimethod identification of microelasticity and hardness, Mech. Adv. Mater. Struct., 15376532 0 (0) (2021) 1–12, https://doi.org/10.1080/15376494.2021.1941450.

[46] K. Durst, M. Göken, H. Vehoff, Finite element study for nanoindentation measurements on two-phase materials, J. Mater. Res., 0884-2914 19 (1) (2004) 85–93, https://doi.org/10.1557/jmr.2004.19.1.85.

[47] E. Parzen, On estimation of a probability density function and mode, Ann. Math. Stat. 33 (3) (1962) 1065–1076, https://doi.org/10.1214/aoms/1177704472.

[48] Y.-C. Chen, A tutorial on kernel density estimation and recent advances, Biostat. Epidemiol. 1 (1) (2017) 161–187, https://doi.org/10.1080/24709360.2017.1396742.

[49] A.Z. Zambom, R. Dias, A review of kernel density estimation with applications to econometrics, Int. Econ. Rev., 1308-8793 5 (1) (2013) 20–42.

[50] S.J. Sheather, Density estimation, Stat. Sci., 08834237 19 (4) (2004) 588–597. URL http://www.jstor.org/stable/4144429.

[51] B.W. Silverman, Density Estimation for Statistics and Data Analysis, Chapman & Hall, 11 New Fetter Lane, London, 1986, ISBN 0412246201.

[52] N. Terashima, K. Kitano, M. Kojima, M. Yoshida, H. Yamamoto, U. Westermark, Nanostructural assembly of cellulose, hemicellulose, and lignin in the middle layer of secondary wall of ginkgo tracheid, J. Wood Sci., 14350211 55 (6) (2009) 409–416, https://doi.org/10.1007/s10086-009-1049-x.

[53] H. Kariem, M.-I. Pastrama, S.I. Roohani-Esfahani, P. Pivonka, H. Zreiqat, C. Hellmich, Micro-poro-elasticity of baghdadite-based bone tissue engineering scaffolds: A unifying approach based on ultrasonics, nanoindentation, and homogenization theory, Mater. Sci. Eng.: C, 0928-4931 46 (2015) 553–564, https://doi.org/10.1016/j.mSection 2014.10.072.

[54] W. Wang, K. Lu, Nanoindentation measurement of hardness and modulus anisotropy in ni3al single crystals, J. Mater. Res. 17 (9) (2002) 2314–2320, https://doi.org/10.1557/JMR.2002.0339.

[55] C.A. Tweedie, G. Constantinides, K.E. Lehman, D.J. Brill, G.S. Blackman, K.J. Van Vliet, Enhanced stiffness of amorphous polymer surfaces under confinement of localized contact loads, Adv. Mater., 09359648 19 (18) (2007) 2540–2546, https://doi.org/10.1002/adma.200602846.

[56] M.S. Bobji, S.K. Biswas, Deconvolution of hardness from data obtained from nanoindentation of rough surfaces, J. Mater. Res. 14 (6) (1999) 2259–2268, https://doi.org/10.1557/JMR.1999.0302.

[57] T. Mori, K. Tanaka, Average stress in matrix and average elastic energy of materials with misfitting inclusions, Acta Metall., 0001-6160 21 (5) (1973) 571–574, https://doi.org/10.1016/0001-6160(73)90064-3.

[58] Y. Benveniste, A new approach to the application of Mori-Tanaka's theory in composite materials, Mech. Mater., 01676636 6 (2) (1987) 147–157, https://doi.org/10.1016/0167-6636(87)90005-6.

[59] Chemical Retrieval on the Web (CROW), Typical Poisson's ratios of polymers at room temperature, https://polymerdatabase.com/polymer%20physics/Poisson%20Table.html, 2022. Accessed: 2022-06-23.

[60] S. Cariou, F.J. Ulm, L. Dormieux, Hardness-packing density scaling relations for cohesive-frictional porous materials, J. Mech. Phys. Solids, 00225096 56 (3) (2008) 924–952, https://doi.org/10.1016/j.jmps.2007.06.011.

[61] A.M. Díez-Pascual, M.A. Gómez-Fatou, F. Ania, A. Flores, Nanoindentation in polymer nanocomposites, Prog. Mater Sci., 00796425 67 (2015) 1–94, https://doi.org/10.1016/j.pmatsci.2014.06.002.
[62] A.H. Ngan, H.T. Wang, B. Tang, K.Y. Sze, Correcting power-law viscoelastic effects in elastic modulus measurement using depth-sensing indentation, Int. J. Solids Struct., 00207683 42 (5–6) (2005) 1831–1846, https://doi.org/10.1016/j.ijsolstr.2004.07.018.
[63] U.D. Cakmak, T. Schöberl, Z. Major, U.D. Cakmak, Z. Major, T. Schöberl, Nanoindentation of polymers, Meccanica 47 (2012) 707–718, https://doi.org/10.1007/s11012-011-9481-6.
[64] G. Hochstetter, A. Jimenez, J.L. Loubet, Strain-rate effects on hardness of glassy polymers in the nanoscale range. comparison between quasi-static and continuous stiffness measurements, J. Macromol. Sci., Part B 38 (5–6) (1999) 681–692, https://doi.org/10.1080/00222349908248131.
[65] B.J. Briscoe, L. Fiori, E. Pelillo, Nano-indentation of polymeric surfaces, J. Phys. D: Appl. Phys., 00223727 31 (19) (1998) 2395–2405, https://doi.org/10.1088/0022-3727/31/19/006.
[66] L. Shen, I.Y. Phang, T. Liu, K. Zeng, Nanoindentation and morphological studies on nylon 66/organoclay nanocomposites. ii. effect of strain rate, Polymer, 0032-3861 45 (24) (2004) 8221–8229, https://doi.org/10.1016/j.polymer.2004.09.062.
[67] S. Beisl, P. Loidolt, A. Miltner, M. Harasek, A. Friedl, Production of micro- and nanoscale lignin from wheat straw using different precipitation setups, Molecules, 1420-3049 23 (3) (2018), https://doi.org/10.3390/molecules23030633.
[68] S. Serna-Loaiza, F. Zikeli, J. Adamcyk, A. Friedl, Towards a wheat straw biorefinery: Combination of organosolv and liquid hot water for the improved production of sugars from hemicellulose and lignin hydrolysis, Bioresour. Technol. Rep., 2589-014X 14 (2021) 100667, https://doi.org/10.1016/j.biteb.2021.100667.